Holographic PIV for Diagnosing Particulate Flows

Ye Pu*, Xiangqun Song* and Hui Meng*
Laser Flow Diagnostics Laboratory
Mechanical & Nuclear Engineering Department
Kansas State University
Manhattan, KS 66506

Abstract

To study the effect of turbulence on particles in a particulate two-phase flow, it is important to be able to measure the three-dimensional (3D) positions and velocities of particles. While such experimental capability has been lacking in the past, Holographic PIV (HPIV) is emerging as a 3D measurement technique to fill in this blank. The development of HPIV was originally motivated from the need to map out turbulent flow fields. We demonstrate that besides giving flow velocity field on 3D grids as a result of correlation (spatial averaging), our off-axis HPIV technique can further provide positions and velocities of individual particles, whether seeded or inherent in the flow. Such information on individual particles opens a new arena for the utility of the HPIV technique – a 3D diagnostics tool for the disperse phase. In the present experiment, an isotropic turbulent flow was generated using eight identical fans in an airtight turbulent chamber, and aluminum powder of 20 microns was added in the chamber as particles. A fully automated off-axis HPIV system based on an injection-seeded dual-pulsed YAG laser and 3D data processing software was used to measure the particulate phase in the chamber. The validity of particle centroid finding and velocity extraction was established via computer-generated particle images dispersed in a rotating flow. Results show that the holographic system is capable of processing a huge number of particles with high accuracy. In the actual holographic measurement of the turbulence chamber, 3D *individual* particle positions, shapes, and velocities were obtained by analyzing a pair of instantaneous holographic images recorded in rapid succession. The true 3D instantaneous experimental data demonstrate for the first time that HPIV technique is a powerful diagnostic tool for particulate flow.

1. Introduction

The measurement of 3D individual particle positions, shapes, sizes, and instantaneous velocities in a turbulent flow plays an important role in multiphase flow research and related industrial applications such as powder processing, sprays, and aerosol transports. In many industrial processes, particle positions and movements in various types of airflow need a reliable instrument to characterize. Meanwhile in the research of particulate flows, detailed measurements with three-dimensional (3D) volumetric information of the particles are critical to modeling particle behavior in turbulence. For example, to validate models for calculating particle collision rate (Sundaram and Collins 1997; Hu and Mei 1998), it is necessary to know particle radial distribution (from particle position) and relative velocity distribution. Due to limitations of the previous experimental techniques, there has been a lack of capability to measure 3D particle positions and velocities except for extremely low density (Kasagi *et al*. 1995; Song *et al*. 1996). Recently matured Particle Image Velocimetry (PIV) provides a possible solution to such measurement, albeit in the two dimensions (2D). Stereoscopic PIV (SPIV), which is commonly considered a 3D extension of PIV, provides three components of the flow velocities confined in a thin slice of moving fluid medium (Arroyo & Greated 1991; Prasad & Adrian 1993; Lecerf *et al*. 1999). It employs the statistical average (correlation) of particles in two separate viewing angles before combining the averaged 2D vectors into 3D vectors, thereby losing information about individual particles. Even if one circumvents this problem by resorting to particle tracking instead of correlation, the information attainable with PIV is only limited in the laser sheet thickness. For the complete 3D measurements, Holographic PIV (HPIV) appears to be the only solution.

---

* Present address:
Laser Flow Diagnostics Laboratory, Dept. of Mechanical and Aerospace Engineering, SUNY Buffalo, Buffalo, NY14260

By capturing the phase information of light waves from the object of interest, holography is an intrinsic instantaneous 3D imaging process that offers an enormous storage capacity suitable for 3D information recording. It is thus inherently a better solution to 3D measurements than any other available technique. HPIV records the 3D information of a large quantity of particles in a fluid *volume* on a hologram instantaneously and then reconstructs the particle images in a 3D space. From the reconstructed image field, we can retrieve the 3D positions (as well as size and shape information) of these particles. Furthermore, by finding the 3D displacements of the particles in the image volume between two exposures separated by a short time lapse, the instantaneous 3D velocities of these particles in the volume can also be obtained. It is interesting to note that HPIV was developed for the purpose of mapping 3D (single-phase) turbulent flows (Barnhart *et al.* 1994; Meng and Hussain 1995; Zhang *et al.* 1997; Pu and Meng 1999). Yet, the inherent power of HPIV for diagnosing the disperse phase in turbulent flow is yet to be explored. It appears that no measurement system, except for HPIV, is currently available for characterizing 3D particulate flow effectively, while retaining the ability to track individual particles. Hence, we set out to extend the capability of our current HPIV technique to particulate flows. As a first step, we concentrate on characterizing the disperse phase separately from the continuous phase, with the plan to advance our measurement capability to both phases simultaneously in the next step. In this paper, we describe the configuration of our off-axis HPIV system, techniques used to extract the particle positions and velocities, and procedures for their validation. We then describe a preliminary application of our technique to the measurement of particles in an isotropic turbulence generated in a confined chamber. The experimental set-up of the turbulence chamber is also depicted in the paper. The profound rationale and detailed description of the off-axis HPIV system can be found in the work of Pu & Meng (1999).

2. Off-axis HPIV Technique

Based on the off-axis holographic principle, we implemented a fully automated experimental off-axis HPIV, which employs 90-degree scattering, dual reference beams, *in-situ* reconstruction, and novel 3D data processing algorithms. The high image signal to noise ratio (SNR) achieved by the off-axis configuration alleviates the need for de-noising in the data processing stage and thus greatly improves the overall processing speed. The high SNR also brings a highly efficient, yet simple implementation of a centroid finding algorithm. By utilizing only particle centroid locations instead of raw images, a compression ratio of several orders has been achieved. At the core of HPIV data processing, a fast Concise Cross Correlation (CCC) algorithm for velocity extraction has been implemented, which works on particle centroids, thereby drastically improving processing speed over conventional cross-correlation. While correlation results are always statistical averaging of particle groups, with our approach the “spatial resolution” of velocity field can be further refined by pairing individual particles in the correlation sets while using CCC results as a reference, achieving super resolution (Keane, *et al*. 1995). In a slightly different light, thus paired vectors are actually individual particle velocities. The positions of these particles are already extracted through centroid finding. Such information on individual particles opens a new arena for the usefulness of our off-axis HPIV technique. In this section we describe the HPIV system in detail.

2.1 Recording

Recording of particle images is the first step in HPIV measurement. Illustrated in Figure 1 is the optical configuration for off-axis HPIV recording of a particulate flow. An injection-seeded dual Nd:YAG laser (Spectra-Physics PIV-400) is employed, which gives a pair of temporally and spatially separated laser pulses, each of 8ns duration, at a repetition rate of 10Hz. Thus, the system is capable of double exposure to provide particle velocity measurement. For particle location information only, single exposure would suffice. However, in most modeling efforts of particulate flows, particle velocity is critical. Hence, we assume that velocity measurement is necessary throughout this paper.

As in regular PIV applications, the double pulse separation Δt is adjusted according to the estimated flow speed. The two laser units contained in the dual YAG laser system are fired by a multi-channel digital delay generator. The addition of injection seeding to the standard PIV-400 laser guarantees sufficient coherence length (over a meter). The increased coherence length enables high-quality off-axis holographic recording of a large volume while allowing unmatched optical path lengths between object and reference beams. To ensure the stability of injection seeding operation, the pulsed laser system has to fire constantly during the recording process, and hence a pair of high-energy shutters operated through a synchronizer are used to generate a single pair of laser pulses. The synchronizer assures each shutter to pass one and only one laser pulse each time. Each laser head emits a beam, which, after passing through a shutter and a pair of high-energy mirrors (HEM), is split into two parts by a partial reflection mirror which works as a beam splitter (BS). The majority of the energy (80%) from each beam is reflected and used for illumination. The two illuminating beams, very close to each other, are combined at a common receiving HEM. The slight angular misalignment between the two beams becomes negligible after they pass through the illuminating beam expander. The transmitting part of each laser beam through the BS is further manipulated by a variable beam splitter (VBS), which consists of a pair of half-wave plates (WP) and a polarizing beam splitter (PBS). With the two VBS, it is possible to adjust the intensity of the reference beams and thus the reference-to-object intensity ratio. Evidently, the beam handling unit (enclosed by dashed line on the bottom-right corner of Figure 1) produces three output beams: two separate reference beams (Reference 1 and 2) and one combined illuminating beam. It actually works as a multiplexer during double exposure: the illuminating beam is double pulsed, while the two reference beams are alternately single pulsed. This dual-reference-beam design provides angular separation of the reference beams for the double-exposure hologram, so that the two holographic images can be reconstructed alternately in time.

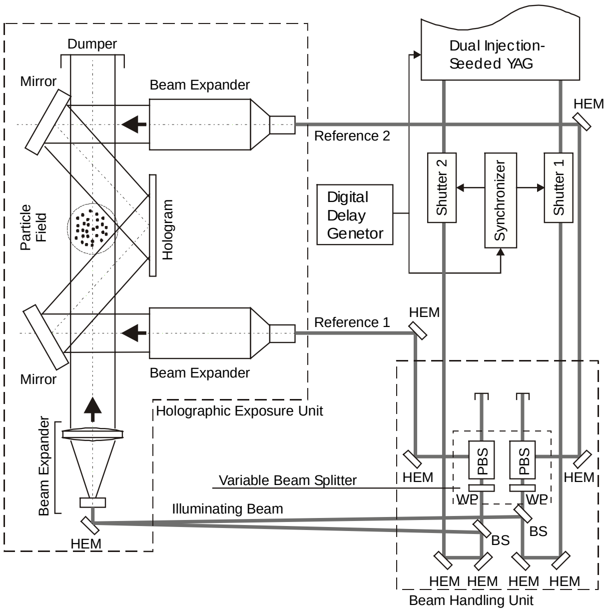

Figure 1: Schematic of off-axis HPIV recording of the particle field. The two laser beams from the injection-seeded dual YAG laser, separated by a short time interval, are splitted by the beam handling unit into 3 beams: The illuminating beam, reference 1 and reference 2. The holographic plate is placed with the emulsion side facing the particle field. A 3D region of the particle field is illuminated, and their 90-degree scattering is recorded on the hologram. A pair of high-energy shutters and a synchronizer are utilized to produce single shots while keeping the laser running to maintain its coherence.

2.2 Reconstruction

After the hologram is recorded and chemically processed, the 3D particle information contained within must be reconstructed optically. To minimize aberrations which is important for achieving high SNR, in our system the hologram is reconstructed *in situ*, where exactly the same laser and the same reference beams used for recording are employed. As shown in Figure 2, the hologram reconstruction system shares the same optics as the recording system, except that the object illustrating beam is blocked since it is no longer needed during reconstruction. The developed hologram containing interference fringes is now placed back at the original position, albeit with the film emulsion facing opposite to that of recording, such that each reference beam incident on the hologram becomes the complex conjugate of that used in recording. In this way, an unscrambled real image of the 3D particle field is reconstructed on the emulsion side, *i.e.*, on the opposite side to the flow field.

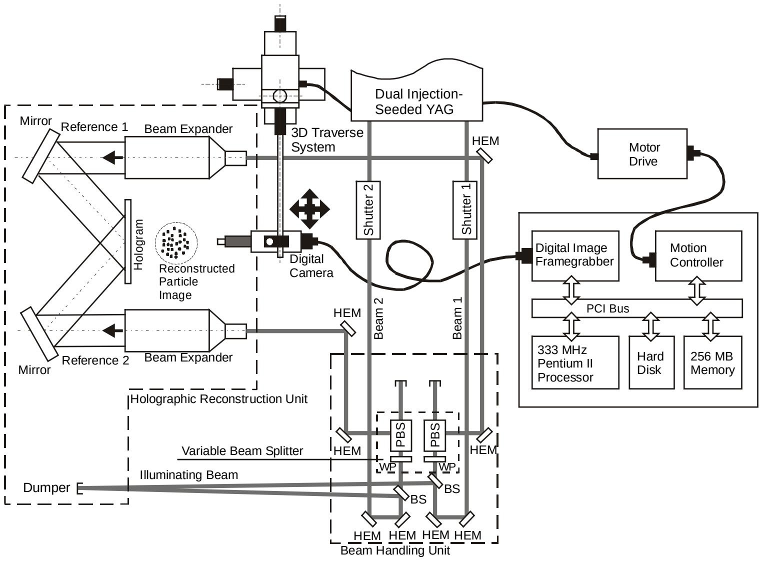

Figure 2: Schematic of off-axis HPIV reconstruction (*in situ*). The hologram is placed at the original location where it is recorded, albeit with emulsion side facing opposite to the reference beam, forming a real image of the particle field on the opposite side. A computer controls the traversing system to move the digital CCD camera in three directions and acquire images plane by plane.

Now that a frozen 3D particle field from each exposure is reconstructed continuously, it can be interrogated with a planar imaging device to be converted into digital form. A high-resolution digital CCD camera mounted on a 3D traversing system (Daedal-Parker) is employed to transfer the reconstructed holographic image field. The camera sees only a small area of a thin slice at a time. The 3D image field is interrogated slice by slice, and area by area. The entire particle field is thus decomposed into many 3D Interrogation Cells (IC), similar to the 2D Interrogation Spots (IS) in planar PIV. The pitch in depth direction, *i.e*. the distance between adjacent slices must be small enough to resolve particle images along the depth. The IC size affects the measurement accuracy and processing speed, as well as the SNR of the acquired image. A larger IC size enables faster processing, but it also leads to a longer effective depth of focus of the particle image as seen by the CCD camera. This is because in order to increase the camera viewing area (by zooming out), the effective N.A. of the objective lens on the CCD camera must be reduced. The increased depth of focus leads to interference from out-of-focus particle images, producing random-spot or speckle noise. In this way, the overall image SNR is degraded. Therefore a compromise between the processing speed and the measurement accuracy have to be compromised.

Data acquisition and processing are fully automated and controlled by a PC. A PCI digital image framegrabber is hosted in the computer to perform image capturing, and a motion controller is also installed to position the camera through the 3-axis traverse system. Image acquisition and camera movement are synchronized with the laser pulses to ensure data integrity. Data processing is completed on the fly, given that the processing is fast enough to follow the image acquisition and camera positioning. A speed of approximately one pair of image planes per second is achieved by the system.

2.3 Data Processing

Figure 3 is a schematic diagram of data processing in our off-axis HPIV system. Digital images captured by the CCD camera are transferred into the system memory in the host computer via the framegrabber. The scanned 3D particle images contain a tremendous amount of data; When the particle size and shape are not among the objectives of measurement, we can compress the data to particle centroid locations. The centroid finding process not only reduces the amount of data by 4 to 5 orders of magnitudes (depending on the particle density), but also enables the application of the CCC algorithm, a novel technique for particle velocity extraction.

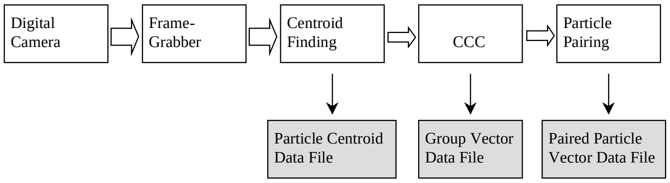

Figure 3: Data flow chart during processing with Concise Cross Correlation (CCC) and particle pairing.

2.3.1 Centroid finding

It is well recognized that the centroid finding process is the bottleneck of the processing speed. Hence the centroid finding is critical to processing efficiency. Because of the high image quality (*i.e.* the high image SNR) of the off-axis holography based on 90-degree particle scattering, no de-noising operation is needed in the centroid finding process. This greatly improves the overall processing speed.

In the digitized image frames an image of a particle is a 3D cluster of pixels with high intensity. Since intensity peak of a particle image is typically located at its geometric centroid, a simple intensity-weighted-mean procedure (described below) provides the centroid coordinate, which is recorded in a list. Thus its 3D centroid location can be calculated according to the intensity-weighted-mean coordinates:

$$\begin{aligned} x_c &= \sum_{m=1}^{n} x_m I_m \Big/ \sum_{m=1}^{n} I_m \\ y_c &= \sum_{m=1}^{n} y_m I_m \Big/ \sum_{m=1}^{n} I_m \\ z_c &= \sum_{m=1}^{n} z_m I_m \Big/ \sum_{m=1}^{n} I_m \end{aligned} \tag{1}$$

where n is the number of pixels in one particle image.

To extract centroids, pixels making up the same particle images must be clustered to apply Eq. (1), and noise pixels must be filtered out. The process consists of intensity thresholding and centroid computation, followed by further noise filtering based on 3D intensity summation of particle images. At first, an appropriate intensity threshold is set to separate particles from the backgroud. Then a list of particle centroids is created and updated throughout the search in the image volume. Each element in the centroid list corresponds to a particle image, consisting of the 3D coordinates of the centroid and total intensity of the pixel cluster. During the process, the first pixel found above the intensity threshold becomes the first element in the list, and subsequently all other pixels in the image field are searched to build the centroid list. At any step, a pixel with intensity above the threshold is compared with other elements in the list. If it is found to be in the proximity (within 8 pixels in x- and y- direction and 4 planes in z-direction) of an existing centroid in the list, it is considered a part of the same particle image. The data of this centroid is updated according to Eq. (1) to accommodate the new member in the cluster. If it is not in the proximity of any centroids, it is added to the list as a new particle centroid.

Even after the thresholding, the extracted centroid file may still contain noise, or “false particles”. This noise can be further reduced through CCC. We will see that CCC has certain tolerance to “false particles”, and unpaired particles can be discarded from the centroid file.

As we perform image scanning and centroid finding, the intensity of the laser beam used to reconstruct the hologram fluctuates from pulse to pulse. This fluctuation is translated into intensity variation between interrogation cells and between different planes within the same 3D particle image, affecting the criteria of intensity threshold and thus affecting accuracy of particle centroids. To overcome this problem, we employ an adaptive threshold calculated based on the histogram of intensity in a plane that the CCD camera captures. Illustrated in Figure 4 is a typical intensity histogram obtained from a plane in the reconstructed image. The particle images occupy the pixels with high intensities, which appear to be a peak on the high intensity side of the histogram. Statistically they consist of an almost constant percentage of the whole image pixels. Since the laser intensity fluctuation has little effect on the profile of the histogram but only shifts it as a whole, we can set the intensity threshold at a certain percentage of the total pixels. Immediately after each image is acquired by the computer, its histogram is computed. The threshold is then calculated by counting pixels from the highest intensity down to the lowest side until a fixed percentage of pixels are included.

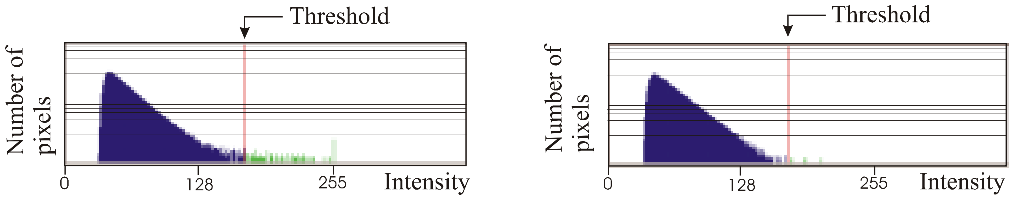

Figure 4: Intensity histogram of one acquired image plane in a logarithmic scale. (a) With particle images. There is a small peak at a high intensity value (255). Statistically the percentage of pixels in such a small peak is constant for the entire volume of one hologram. (b) Without particle images.

The accuracy of centroid locations is asymmetric along the three directions. In x- and y-directions (camera sensor plane) pixels are usually a few microns apart from each other. In z-direction, however, sample points correspond to discrete image planes, whose pitch distance (between two adjacent planes) is typically 50-200μm, depending on the image depth of focus and desired data processing speed. Therefore the z-coordinate in the centroid finding requires a “sub-pixel” resolution for higher accuracy.

2.3.2 Concise Cross Correlation (CCC) algorithm

After the centroid file is established, the 3D positions of particles are given, from which statistics of particle distribution can be extracted. To further obtain particle velocities, we correlate two particle centroid files corresponding to the two exposures made on the hologram. Here, CCC algorithm is the key to velocity extraction. Specifically, CCC gives particle group velocity. Its basic idea comes directly from the primary definition of cross correlation, whose physical meaning is image translation and multiplication/accumulation. To cross correlate a group of particles in two exposures is essentially to match the morphological patterns of the two images. The resemblance between the two patterns depends on the time interval between the two exposures and the velocity gradient of the flow. Therefore, the morphological deformation between the two patterns can be limited to an acceptable level by setting a small enough time interval. It is important to recognize that correlation (pattern matching) procedure described above can be performed on particle centroid coordinates. Since most pixels in the acquired CCD image are dark background, the whole image data can be represented by a sparse matrix by taking all the particle centroids in the image as 1 and the background as 0.

In our implementation of correlation, we take two groups of particle centroids, whose 3D coordinates are extracted from a pair of images in the double exposure. Keeping one of them fixed in its original place, we translate the other one in the 3D space and compute their correlation intensity. The displacement yielding the highest correlation peak is considered the displacement of the particle group and is the correlation output. Figure 5 illustrates how CCC works.

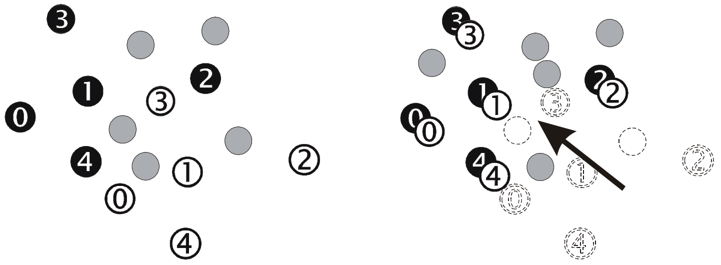

Figure 5: Schematic showing the principle of Concise Cross Correlation (CCC). (a) Two groups of particle centroids (dark and white balls) correspond to two exposures. Gray balls represent noise. (b) During the calculation one group of centroids (white balls) and some of the noise are translated in space, until their morphological pattern best matches that of the other group (dark balls).

After CCC finds the mean displacements of particle groups, individual particles are paired. In each Interrogation Cell, the first set of particle centroids is shifted towards the second by the mean displacement calculated from CCC. Now that there is no net displacement of the particle group but only net deformation between the two exposures, if the deformation is within a limited (as usually required by PIV), pairing can be accomplishable on the basis of closest distance. This pairing process produces out of one IC hundreds of vectors corresponding to individual particles.

2.3.3 Measurement accuracy and validation

The accuracy of HPIV largely depends on the data processing, or specifically speaking, the centroid finding and the CCC algorithm including particle pairing. A displacement vector from particle pairing can be expressed as:

$$\mathbf{s} = \mathbf{s}_{trans} + \mathbf{s}_{deform} \tag{2}$$

where $\mathbf{s}_{trans}$ is translational mean displacement of the particle group obtained by correlation, and $\mathbf{s}_{deform}$ is individual particle displacement corresponding to the morphological deformation of the particle pattern. This deformation is contributed by both the velocity gradient within the particle group and error in particle centroid extraction. Therefore the measurement error of each paired vector can be expressed as:

$$\varepsilon = \varepsilon_c + \varepsilon_p \tag{3}$$

where ε_c is correlation error, and ε_p is pairing error. It is important to realize that the correlation result acts only as a reference for individual particle pairing; in other words, it points the rough amount and direction that the particle group needs to shift to find the partners for the particles. Even if the mean displacement is off to some degree, as long as it's not "grossly wrong", the particles will find their matches. To assure that the correlation is not "grossly wrong", we require that

$$\varepsilon_c < \frac{d}{2} \tag{4}$$

where d is the mean particle distance. As long as Eq. (4) is satisfied, the closest-distance method will produce statistically correct pairing. The mean displacement does not appear in the individually paired vectors, and its error does not propagate to the paired vectors. Hence, in the pairing result, the only error left is ε_p, which is determined by the uncertainty of the particle centroids.

To test measurement accuracy, two types of simulations were performed. The first aims at the correctness of the correlation results, while the second explores the uncertainty of centroids, which is responsible for error of paired vector, at the premise of correct correlation. Thus the final measurement accuracy can be determined by the statistics of the results form the two types of numerical simulations.

The first simulation is to quantify the probability of correct correlation results, or the "correctness", of CCC under various conditions. Incorrect correlation is mainly caused by "false particles" and morphological deformations of particle groups. In correlating double-exposure there are always particles in one group that do not have matching particles in the other group due to weak particle images, contribution of noise, or particles moving out of IC. These are referred to as "false particles". On the other hand, velocity gradients of the fluid cause the morphological pattern of the centroids to change between the two particle groups. In the simulation we generate one group of centroids that are randomly distributed in a volume, then translate them by a given distance, individually shift each centroid by a small but random amount to mimic deformation, and add a certain number of false particles to form the second group. The correlation result is then compared with the generated translation to determine if the result is correct.

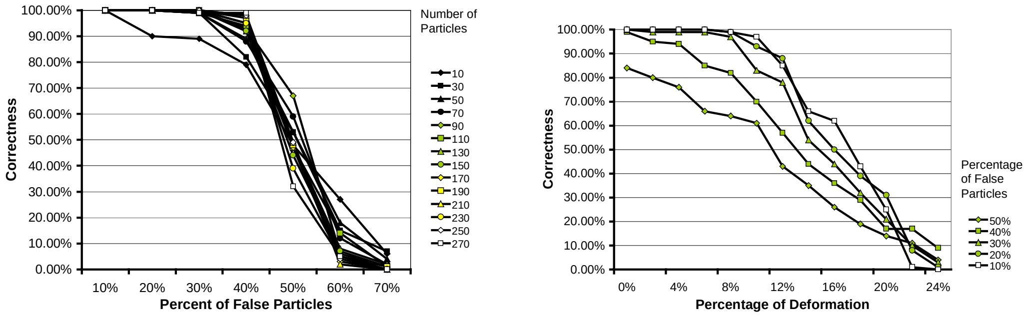

Figure 6: Correctness of CCC algorithm tested by simulation: (a) Correctness vs. percentage of false particles (noise) for various numbers of particles. Average deformation is 2%. Note that with as much as 40% false particles the correctness still reaches 80%. (b) Correctness vs. the amount of particle group morphological deformation (as a percentage of IC size) for various levels of presence of false particles.

Illustrated in Figure 6 (a) is the correctness of CCC as a function of the percentage of false particles. Performance under a wide range of densities (10 ~ 270 particles per IC) has been simulated. In most cases with as many as 40% false particles the correctness is still above 80%. Figure 6 (b) shows the correctness of CCC as a function of morphological deformation. In the figure deformation is indicated as percentage of IC size. Satisfactory results can be obtained by CCC even at as high as 10% deformation.

The second simulation explores particle pairing error, which is contributed by centroid finding uncertainty. Numerically generated particles are added to a simulated flow. They randomly distributed in a given volume and projected onto a series of planes throughout the volume. The image planes are then fed to the centroid finding and CCC algorithms including particle pairing. The results from the algorithms (centroids and vectors) are compared with those initially generated data. To obtain statistical result, a large number of simulations were performed.

In each simulation, two groups of particles are generated, where the second group is transformed from the first group of particles according to a spiral motion. Figure 7 shows how the particles and their motion are generated. Figure 7 (a) shows the geometry of the simulated spiral motion – a solid-body rotation about an axis oriented at (θ ,ϕ) where θ and ϕ are arbitrary angles, plus a translation *s* along the rotation axis. Digitally generated particles are randomly dispersed in 3D space to follow the spiral motion of the flow. The volume is scanned plane by plane along z-axis. The IC size employed in the simulation is 2×2×2 mm^3, and the z-direction pitch distance is 50 or 100 µm. Figure 7 (b) depicts how a single particle image is generated. The particle image intensity is modeled as a Gaussian distribution:

$$I(x,y,z)=I_0\exp\left(-\frac{x^2+y^2}{r_0^2+z^2\tan^2\alpha}\right) \tag{5}$$

where *x*, *y*, and *z* are the relative coordinate to the focal point of the particle image, I_0 is the center intensity at the focal point, r_0 is the size of the particle, and α is the angular aperture of the particle image. The effective edge of the image section varies along z-axis according hyperbolically, which is rather realistic according to the holographic reconstruction. Shown in Figure 7 (c) is a single simulated particle image on consecutive planes.

It is clear that the simulated 3D dispersed particle image field incorporates both the effect of individual particle intensity distribution, to allow centroid finding to be tested, and drastic velocity gradients, to put the CCC algorithm to test. We applied the entire HPIV data processing procedure (save the physical image acquisition) to this simulated “particulate flow” and extracted particle centroids and velocities. Figure 8 shows a snapshot of the extracted particle velocity field from the simulated images, where gray and black dots represents particle centroids extracted from the first and second exposure respectively. This extracted particle field was compared with the simulated particle field and error was determined.

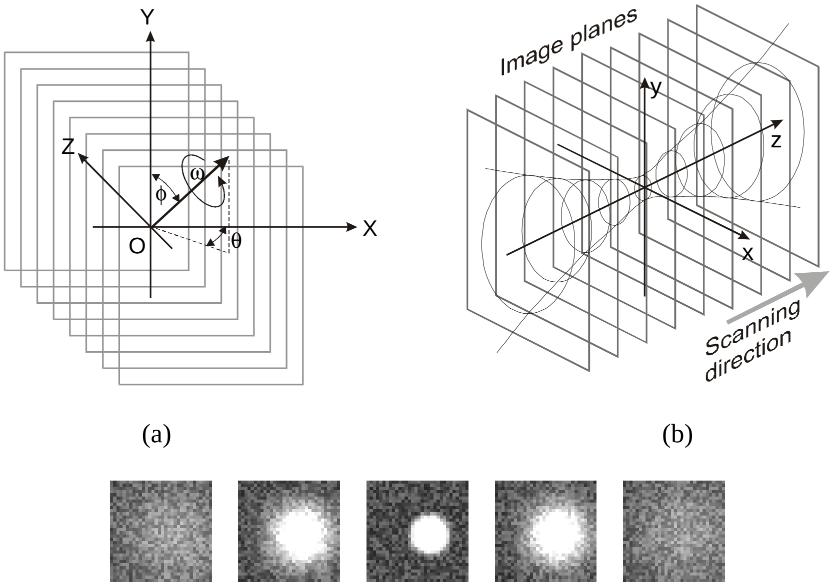

(a) (b)

(c)

Figure 7: Simulation of particle images. (a) Geometry of simulated spiral motion flow (solid-body rotation about an axis oriented at (θ ,ϕ) where θ and ϕ are arbitrary angles, plus translation along the rotation axis). Digitally generated particles are randomly dispersed in 3D space to follow the spiral motion of the flow. The volume is scanned plane by plane along z-axis; (b) Simulation of a single particle image as reconstructed from a hologram. Based on real situation, the intensity distribution is assumed to have a hyperbolic profile along z-axis; (c) A simulated single particle image on consecutive planes from out-of-focus to in-focus to out-of-focus again.

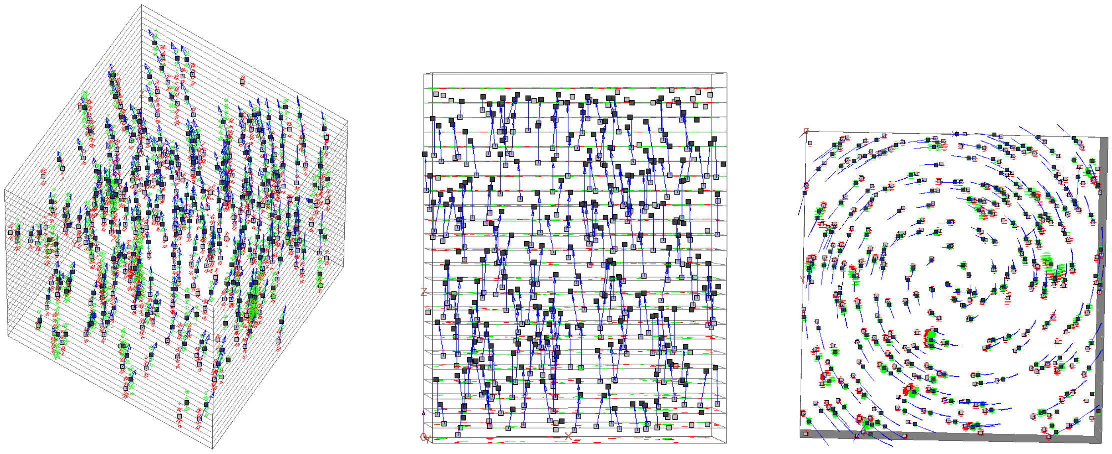

(a) (b) (c)

Figure 8: Particle centroids and velocities extracted from the simulated particle field for ϕ=0. Gray and black dots represent particle centroids in each group. The arrows indicate velocities. Note that the simulated flow field has a spiral motion. (a) perspective view. (b) side view. (c) top view.

For a reliable assessment of centroid uncertainty and velocity mapping error, a large number of simulations with various ω and s at different particle density N were performed so as to obtain statistical mean of the uncertainty. Due to the sparser planes in z-direction compared with the pixels on x-y plane, or the CCD sensor plane, uncertainty in z-direction (δ_z) is much more severe than that in x- and y-direction (δ_x and δ_y). Figure 9 shows distribution of δ_z at two values of z-direction pitch distance (d_p). Note that δ_z at d_p = 100 μm spans much wider than δ_z at d_p = 50 μm. It is clear that 50μm pitch gives much smaller δ_z than 100μm. However, setting d_p to 50 μm doubles the data processing time compared to d_p = 100 μm. Illustrated in Figure 10 is the mean centroid uncertainty as a function of particle density. With increasing particle density, the chance of having agglomeration increases, making centroid extraction less accurate. The mean error of displacement or velocity as a function of density is shown in Figure 11. Note that this error is actually lower than the centroid uncertainty, which is a result of a strict culling process (*i.e.* centroids with large positional error is less likely to be paired and is therefore less likely to appear in the final results).

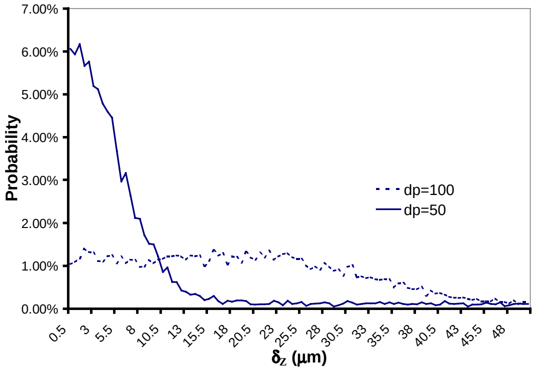

Figure 9: Distribution of mean uncertainty of centroid δ_z at two values of z-direction pitch distance (d_p). Note that δ_z at d_p = 100 μm spans much wider than δ_z at d_p = 50 μm. However, setting d_p to 50 μm doubles the data processing time compared to d_p = 100 μm.

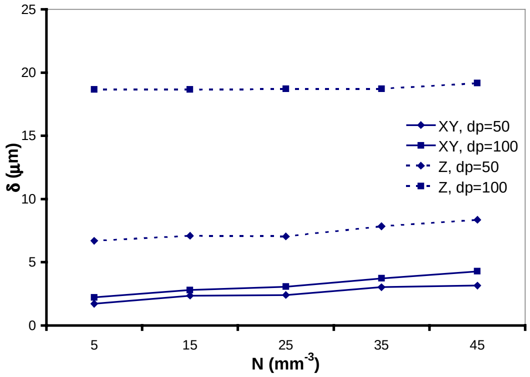

Figure 10: Mean centroid uncertainty as a function of particle density. Due to the chances of having agglomeration increases with increasing seeding density, the uncertainty also increases, making centroid extraction less accurate at high seeding densities than that at low seeding densities.

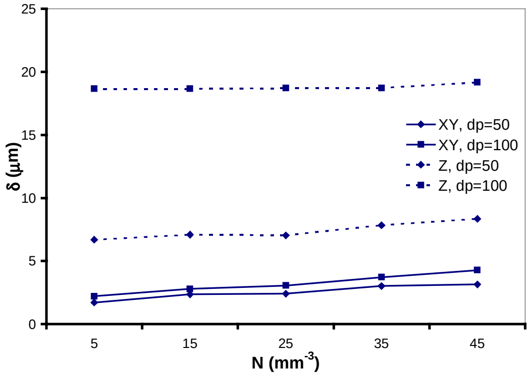

Figure 11: Mean error of displacement or velocity as a function of particle density. Because of the strict culling process in the pairing, centroids with large uncertainty is less likely to be paired and is therefore less like to appear in the final results. Thus this error is actually lower than the centroid uncertainty.

3. Particle Measurement

To generate isotropic and homogeneous turbulence with zero mean velocity in a laboratory, we follow the work of Birouk *et al*. (1996). In our turbulence chamber, eight blowing fans are set in corners of the cubic box in such a way that a 3D symmetry of the flow field can be achieved. The flow field inside the turbulence chamber has been investigated in our lab using PIV. The PIV measurements of the three r.m.s. fluctuating velocity components show that, in a roughly spherical region of 4 cm diameter in the center of the chamber, the turbulent flow is isotropic with a quasi-zero mean velocity.

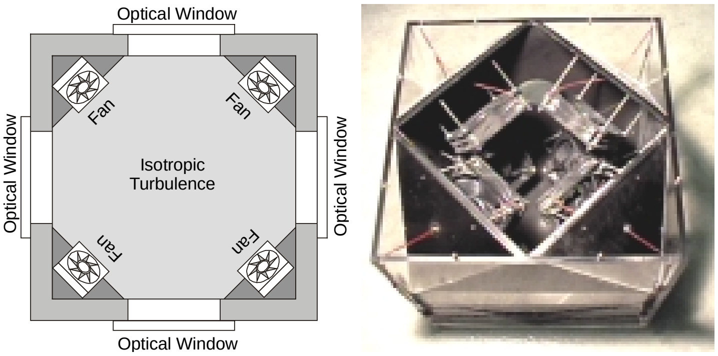

(a) (b)

Figure 12: Turbulence chamber used in our experiment. (a) Schematic drawing; (b) A photo of the chamber with upper lid removed.

As illustrated in Figure 12, the chamber is a cubic box made of one-cm thick Plexiglas plates with an external dimension of $40\times40\times40\text{cm}^3$. Inside the chamber, the corners are obstructed with some equilateral triangular plates in order to create a polyhedron with 14 faces, among which eight faces are these triangular plates, and the other six faces are parts of the initial square faces of the cube. Thus in this way an internal spherical volume is approached. Transparent windows on the wall of the chamber allow optical access. Using eight identical electrical fans, isotropic turbulence inside the chamber is generated. Computer-cooling fans are used, each of which has five blades with an inner diameter of 5cm. Each of the eight fans is mounted on a triangular plate in each corner so that the configuration of all of them is fully symmetrical. The rotation speed of the fans can be varied over a whole range from 500 ~ 3000 rpm.

To study the interaction of turbulence with particles, 20-μm aluminum particles were dispersed in the fan-forced air flow in the chamber. The chamber is placed in the "particle field" location in the HPIV recording setup shown in Figure 1 and imaged with a pair of laser pulses on a holographic plate. The developed hologram is placed back in Figure 2, and the reconstructed 3D particle image field is scanned with the CCD camera while centroid finding and CCC velocity mapping are performed on the fly. Shown in Figure 13 is a typical plane of reconstructed particle images in a $9\times9\text{cm}^2$ area out of the 3D holographic image volume, viewed by the CCD camera.

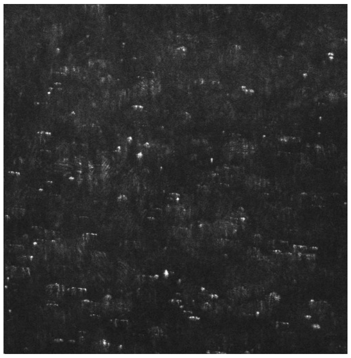

Figure 13: One plane of reconstructed particle images in a $9\times9\text{cm}^2$ area out of the 3D holographic image volume, viewed by the CCD camera.

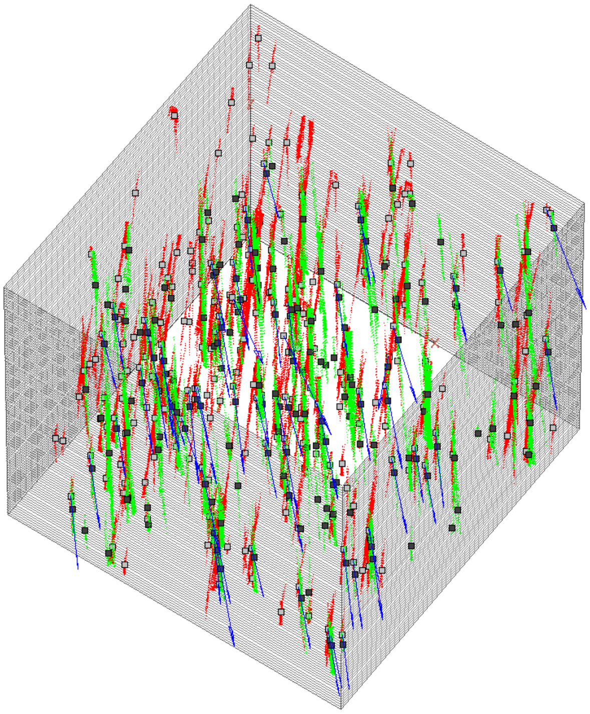

(a)

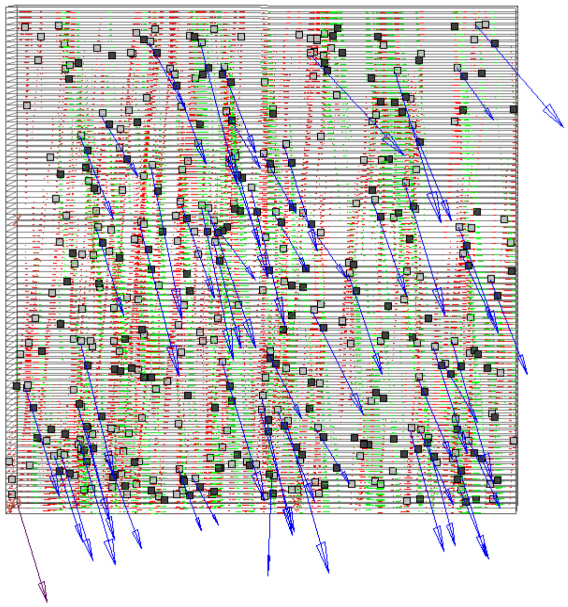

(b)

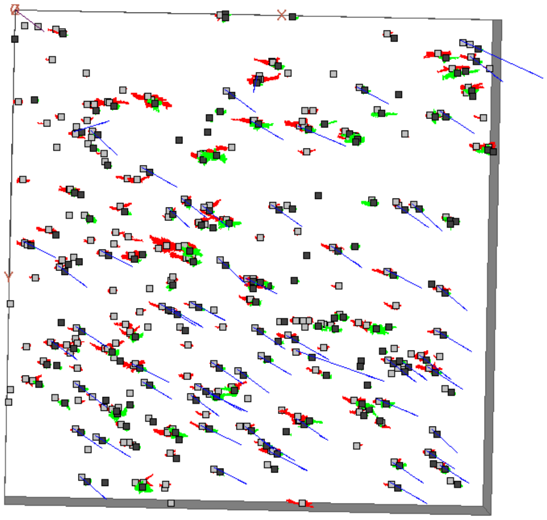

(c)

Figure 14: Holographic measurement of instantaneous 3D particle centroids and velocities in a single IC, obtained from the turbulence chamber. Red and green spheroids represent reconstructed 3D particle images at first and second exposures, respectively. Gray and black dots represent corresponding particle centroids extracted from each exposure. Arrows indicate particle velocities. In the experiment, IC size is 8×8×8 mm^3, and z-direction pitch distance d_p=100µm. Note that the magnitudes of the arrows are magnified for best observation. (a) perspective view; (b) side view; (c) top view.

Figure 14 demonstrates the experimental results obtained from the hologram of the flow. In the figure, red and green spheroids represent reconstructed 3D particle images at first and second exposures, respectively, and gray and black dots represent corresponding particle centroids extracted from each exposure. Arrows indicate particle velocities. Particle boundaries with elongated shapes due to the depth of focus are also demonstrated in the figure. For clarity of the demonstration of the particle motion, velocity vectors are magnified. In the experiment the IC size is 8×8×8mm^3, and the z-direction pitch is 100µm.

Vectors shown in Figure 14 are not filtered. They contain a few spurious vectors due to the uncertainty of particle centroid caused by the depth of focus, which drastically elongates the reconstructed particle images into slim rods. Despite the complex 3D topology of particle images, however, most particle centroids were extracted correctly by the present centroid finding algorithm. Our results show that the off-axis HPIV technique can be successfully adapted to measurement of 3D individual particle positions and velocities.

4. Summary

In this paper we described an advanced off-axis HPIV system that was successfully applied to a particulate flow in an isotropic turbulence chamber. The system was validated by simulated particle images in a rotating flow and applied to experimental measurement of an isotropic turbulence. True 3D *individual* particle positions and velocities were obtained from the measurement, demonstrating the potential of HPIV as a diagnostics tool for particulate flows.

Acknowledgement

The authors wish to acknowledge the support of HPIV development from the National Science Foundation in the form of a CAREER Award (CTS-9625307) and a Research Equipment Grant (CTS-9700373). They are grateful to Mike Roco and Lance Collins for encouraging them to apply HPIV to particulate flows. Support from Kansas Program for Complex Fluid Flows at Kansas State University, including the loan of the turbulence chamber, is greatly appreciated. They also wish to thank Mr. Matthieu Delahaye at the Laser Flow Diagnostics Lab for his experimental investigation on turbulence chamber.

Reference

1) Arroyo MP and Greated CA (1991) Stereoscopic particle velocimetry. Meas. Sci. Technol. 2: 1181-1186.

2) Barnhart DH; Adrian RJ; Meinhart CD and Papen GC (1994) Phase-conjugate holographic system for high-resolution particle image velocimetry. Appl. Opt. 33: 7159-7169.

3) Birouk M; Chauveau C; Sarh B; Quilgars A and Gökalp (1996) Turbulence effects on the vaporization of monocomponent single droplets. Combust Sci Tech 113 114: 413-428.

4) Hu KC and Mei R (1998) Particle collision rate in fluid flows. Physics Fluids. 10, 4: 1028-1030.

5) Kasagi N, and Matsunaga A, (1995) Three-Dimensional Particle-Tracking Velocimetry Measurement of Turbulence Statistics and Energy Budget in a Backward-Facing Step Flow. Int J Heat & Fluid Flow, 16, 6: 477-485.

6) Keane RD; Adrian RJ and Zhang Y (1995) Super-resolution particle image velocimetry. Meas. Sci. Technol. 6: 754-768.

7) Lecerf A; Renou B; Allano D; Boukhalfa A and Trinité M (1999) Stereoscopic PIV: validation and application to an isotropic turbulent flow. Exp Fluids 26: 107-115

8) Meng H and Hussain F (1995) In-line Recording and Off-axis Viewing (IROV) technique for holographic particle velocimetry, Appl. Opt. 34: 1827-1840.

9) Prasad K and Adrian RJ (1993) Stereoscopic particle image velocimetry applied to liquid flows. Exp Fluids 15: 49-60.

10) Pu Y and Meng H (1999) An advanced off-axis holographic particle image velocimetry (HPIV) system. (submitted to Exp Fluids, to be published).

11) Sundaram S and Collins R (1997) Collision statistics in an isotropic particle-laden turbulent suspension. Part 1. Direction numerical simulations. J Fluid Mech, 335: 75-109.

12) Song X, Yamamoto F, Iguchi M, Koketsu M, Chen G, (1996) 3-D PTV measurement of bubble rising flow in cylindrical vessel, ISIJ Int, 36: 54-57

13) Zhang J; Tao B and Katz J (1997) Turbulent flow measurement in a square duct with hybrid holographic PIV. Exp Fluids, 23: 373-381